



An efficient multi-functional material based on polyether-substituted indolocarbazole for perovskite solar cells and solution-processed non-doped OLEDs

Received 00th January 20xx,
Accepted 00th January 20xx

DOI: 10.1039/x0xx00000x

www.rsc.org/

Runsheng Mai^{a,&}, Xiayan Wu^{a,&}, Yue Jiang^{a,*}, Yuying Meng^b, Baiquan Liu^{c,*}, Xiaowen Hu^d, Jean Roncali^{e,i*}, Guofu Zhou^{d,h}, Jun-Ming Liu^{f,a}, Krzysztof Kempa^{g,a}, Jinwei Gao^{a,*}

We demonstrated an efficient multi-functional material, (*E*)-1,2-bis(5,11-bis(2-(2-ethoxyethoxy)ethyl)-5,11-dihydroindolo[3,2-*b*]carbazol-2-yl)ethane (**BEDCE**), accessible by simple and low-cost solution processing procedure, that could be simultaneously used as an interfacial layer in perovskite solar cells (PSCs) and greenish-yellow light emitter in organic light-emitting diodes (OLEDs). With an excellent morphology and interfacial contact led by its elastomeric and amphiphilic properties, the **BEDCE** layer at perovskite/Spiro-OMeTAD interface in PSCs has significantly improved the short-circuit current and fill factor, enhancing the efficiency from 17.20% to 19.02%. Besides, the first solution-processed non-doped greenish-yellow OLEDs based on elastomeric **BEDCE** show efficiency and luminance of 4.56 cd A⁻¹ and 10320 cd m⁻², respectively, which is among the highest rank. Thus, **BEDCE**, as far as we know, is the first time that a multi-functional material can be appreciated in both OLEDs and PSCs with good performance, showing its promising potential applications for various devices.

Introduction

The interconversion devices between light and electricity based on organic conjugated materials (OCMs) has obtained tremendous attention due to the eco-friendly, solution-processed and easy tuning of those properties of OCMs¹⁻³, such as organic solar cells (OSCs)⁴⁻⁷, organic light-emitting diodes (OLEDs)⁸⁻¹⁰, and organic field effect transistors (OFETs)¹¹⁻¹³, etc. It is well-known that the photovoltaic (PV) process is the reverse of electroluminescence (EL), and the PV and EL processes accordingly require different optical and electronic properties for a source material. Given that light should be absorbed in PV

devices but emitted in EL devices, materials used in a PV device usually have opposite energetic level "ladders" to those used in an EL devices. Therefore, among those enormous OCMs, few of them could be efficiently applied in PV and EL devices simultaneously. In other words, a material may be a good candidate for PV generation but it may not be appreciated as an electrically driven high-quality light emitter. In a more general perspective, searching for efficient multi-functional organic materials favoring both excellent photon-to-charge and charge-to-photon conversions is of great importance. Such a material which could solve multi-problems at the same time is highly preferred for not merely the reduction of overall cost with only one necessary apparatus, but also the possibility of more intelligent and multi-functional devices in future.

In these molecular construction, polycyclic aromatic systems with heteroatoms have received special attention because of those merits, such as good stability, higher charge mobility, better solubility and versatility¹⁴. Among them, indolo[3,2-*b*]carbazole (ICZ) (shown in Scheme 1) is a planar and rigid π -conjugated system consisting of five fused rings with two unsubstituted pyrroles. The good thermal stability and excellent charge-transport properties of ICZ derivatives have led to extensive investigations on the possible applications of these compounds as hole-transport materials (HTM) for perovskite solar cells (PSCs)^{15,16} and as the host in OLEDs^{17,18}, thus providing the possibility to develop its derivatives for multi opto-electronic devices.

^a Institute for Advanced Materials, Academy of Advanced Optoelectronics, and Guangdong Provincial Key Laboratory of Quantum Engineering and Quantum Materials, South China Normal University, Guangzhou 510006, P. R. China.

^b Sun Yat-Sen University, School of Chemistry, Guangzhou, 510275, P. R. China.

^c Luminous Centre of Excellence for Semiconductor Lighting and Displays, School of Electrical and Electronic Engineering, Nanyang Technological University, Singapore 639798, Singapore.

^d Guangdong Provincial Key Laboratory of Optical Information Materials and Technology & Institute of Electronic Paper Displays, South China Academy of Advanced Optoelectronics, South China Normal University, Guangzhou 510006, P. R. China.

^e Moltech-Anjou CNRS UMR 6200, University of Angers, 2 Bd Lavoisier, Angers, 49045, France.

^f Laboratory of Solid State Microstructures, Nanjing University, Nanjing 210093, P. R. China.

^g Department of Physics, Boston College, Chestnut Hill, Massachusetts 02467, USA.

^h Shenzhen Guohua Optoelectronics Tech. Co. Ltd., Shenzhen 518110, P. R. China.

ⁱ Supramolecular Organic and Organometallic Chemistry Center, Babes-Bolyai University, 11 Arany Janos str., 400028 Cluj-Napoca, Romania.

Currently PSCs with more than 22% power conversion efficiency (*PCE*) have been reported^{19–21}, but one of the most important components, 2,2,7,7-tetrakis(*N,N'*-di-*p*-methoxyphenylamine)-9,9-spirobifluorene (Spiro-OMeTAD) has been suffering from stability and cost issue. For example, the high crystallinity of Spiro-OMeTAD limits the full coverage and interconnection of perovskite crystals^{22–24}. Furthermore, the dopant of Spiro-OMeTAD could inevitably diffuse into the perovskite crystals, thus shortening the lifetime of devices^{24–27}. In this context, an intense research activity aiming at the development of new HTMs as alternatives to Spiro-OMeTAD^{28–31}, including carbazole derivatives such as ICZ has been undertaken³². Bao, Leclerc and coworkers have investigated structure-hole-mobility (μ_h) relationships on OFETs based on a series of six ICZ derivatives^{15,33}. Getautis and Nazeeruddin reported two HTMs based on the ICZ block, leading to PSCs with *PCE* of ~15%¹⁶. On the other hand, other star-shaped carbazole derivatives also show promising potential as HTMs^{34,35}. However, it should be mentioned that Spiro-OMeTAD is an exceptional HTM in spite of some deficiencies, and it would be much better to search for alternative strategy for correcting these deficiencies rather than utilizing other potential HTM as replacement. Interfacial engineering is an efficient way to reduce the surface carrier recombination and enhance the efficiencies of PSCs^{36,37}. Recently, PVK and PMMA thin layers have been inserted between Spiro-OMeTAD and active layer in PSCs, enhancing the efficiency by the increased charge-separation process while protecting the device from moisture^{38,39}. Interfacial doping effect is also used to surface passivation and reduce the carrier losses. Li and coworkers employed the electron-acceptor tetrafluorotetracyanoquinodimethane (F4TCNQ) to improve *PCE* from 14.3% to 16.4%⁴⁰.

For the charge-to-photon conversion, in the field of OLEDs, high-quality blue, green, and red emission devices have been fabricated and some of them were commercialized. Nevertheless, less attention has been paid to yellow emission materials and devices, particularly the greenish-yellow emission materials. In fact, until now efficient and bright-yellow OLEDs are usually constructed by host dopant systems⁴¹, which requires precise and complicated fabrication process with high cost on one hand and inevitable microstructural phase separation in many cases on the other hand. Recently, high-efficiency bright-yellow materials and low-cost processing

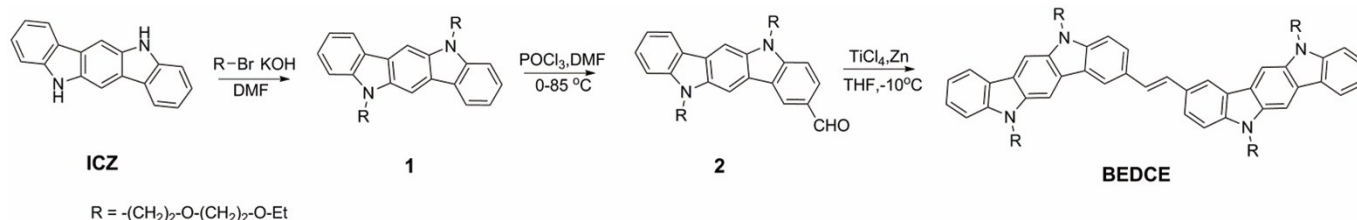
performance of solution-processed OLEDs lags behind that with vacuum evaporation. On account of the potential applications in stage lights, signal lights, and high quality RGBY-TV⁴³, it is urgent to develop novel materials for the efficient and bright solution-processed non-doped greenish-yellow OLEDs.

Here, we report on the synthesis and characterization of an efficient multi-functional ICZ-based material (*E*)-1,2-bis(5,11-bis(2-(2-ethoxyethoxy)ethyl)-5,11-dihydroindolo[3,2-b]carbazol-2-yl)ethane (**BEDCE**), an extended derivative of ICZ on which four oligo-oxyethylene side chains have been introduced at the nitrogen atoms. We demonstrated the critical role of this material in both high-efficiency PSCs and bright greenish-yellow OLEDs accessible by simple and low-cost solution processing procedure. The **BEDCE** layer at perovskite/Spiro-OMeTAD interface in PSCs has significantly enhanced the short-circuit current and fill factor, yielding the best efficiency up to 19.02%. Furthermore, long side chains inhibit the strong π - π stacking of the ICZ blocks, and the first solution-processed non-doped greenish-yellow OLEDs based on elastomeric **BEDCE** show efficiency and luminance of 4.56 cd A⁻¹ and 10320 cd m⁻², respectively, which is among the highest rank. As far as we know, this is the first time that a multi-functional material can be appreciated in both OLEDs and PSCs with good performance, showing its promising potential applications for various devices.

Results

Synthesis, optical, electrochemical and morphology characterization

The three-step synthesis of **BEDCE** is depicted in Scheme 1. ICZ was prepared as previously reported⁴⁴. *N*-alkylation was conducted in the presence of KOH with 2-(2-ethoxyethoxy)ethyl bromide to give compound **1** in 51% yield. Vilsmeier-Haack formylation of compound **1** with DMF, POCl₃ in dioxane gave compound **2** in 75% yield. Finally, the target compound **BEDCE** was obtained in 59% yield by McMurry reaction. The detailed synthesis procedures and NMR and Mass spectrometry of those molecule, including compounds **1**, **2** and **BEDCE** are shown in Supporting Information (Figs S1–S6).



Scheme 1 The Key Synthesis Routes for **BEDCE**.

technique became equivalently important. The solution-processed technique (e.g., spin-coating) offers many merits compared with the vacuum evaporation technology⁴². Yet, the

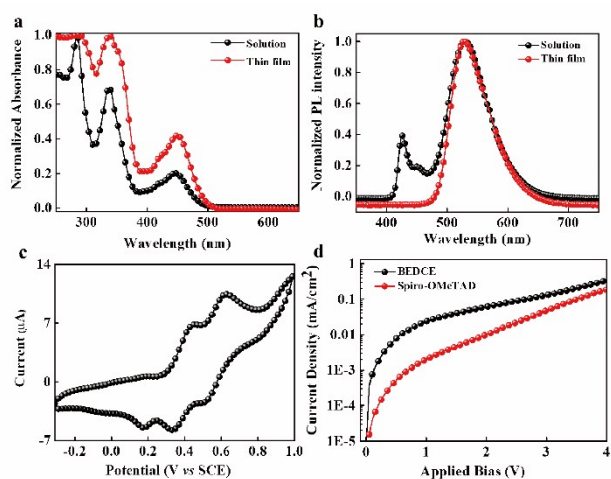


Fig. 1 Optical and electronic properties of BEDCE. a) UV-Vis absorption spectra in chloroform and as thin film. b) Photoluminescence spectra in THF and as thin film. c) Cyclic voltammetry curve in 1 mM in 0.10 M $\text{Bu}_4\text{NPF}_6/\text{DCM}$, scan rate 50 mV s^{-1} , Pt working electrodes. d) SCLC curves for BEDCE (black) and Spiro-OMeTAD (red).

The thermal behavior and stability of **BEDCE** have been determined by differential scanning calorimetry (DSC) and thermal gravity analysis (TGA) (Fig. S7, Supporting Information). The decomposition temperature (T_d) is evaluated to be $\sim 380^\circ\text{C}$, suggesting that **BEDCE** is stable enough for the usage in optoelectronic devices. The DSC trace exhibits a weak exothermic peak at 20°C , corresponding to the glass transition temperature (T_g) which results in an elastomeric material at room temperature, in agreement with naturally amorphous phase. These results indicate that the incorporation of four oligo-oxethylene chains on the nitrogen atoms introduces the large steric hindrance, modulating the strong π - π stacking tendency of the ICZ skeletons.

Fig. 1a shows the UV-Vis absorption spectra of **BEDCE** and the corresponding results, listed in Table 1. The solution spectrum of **BEDCE** exhibits two absorption bands with maxima (λ_{max}) at 284 and 338 nm corresponding to π - π^* transition of ICZ, ICZ vinyl, respectively, followed by a low-intensity band with λ_{max} at 446 nm assigned to the entire π conjugated system. The spectrum of solution-cast thin film shows a broadening of the absorption band with 4–6 nm bathochromic shifts of the absorption maxima. These slight redshifts are the indicative of relatively weak intermolecular interactions. A band gap (E_g) of $\sim 2.36 \text{ eV}$ was estimated from the long-wavelength absorption edge of the solid-state spectrum. Fig. 1b shows the PL spectra of **BEDCE** in tetrahydrofuran (THF) solution and as thin film spun-cast on quartz under monochromatic irradiation at 284 nm. The solution spectrum shows two emission bands with maxima at 426 and 531 nm attributed to the ICZ vinyl unit and π conjugated system the separately, with PL quantum yield (Φ_{PL}) of 88.1%. In the solid-state spectrum, the intensity of the band at 426 nm strongly decreases presumably because of intermolecular interactions, while the band in the 500–600 nm region results in an intense greenish-yellow light.

To examine the electrochemical properties of **BEDCE**, the cyclic voltammogram (CV) of **BEDCE** was recorded in dichloromethane (DCM) in the presence of 0.10 M tetrabutylammonium hexafluorophosphate as the supporting electrolyte. The CV curve presents two quasi-reversible oxidation waves with anodic peak potentials ($E_{\text{pa}1}$ and $E_{\text{pa}2}$) of 0.75 and 0.93 V (Fig. 1c and Table 1). The highest occupied molecular orbital (HOMO) energy level of -5.28 eV was estimated from the onset of the oxidation process while the lowest unoccupied molecular orbital (LUMO) level (-2.91 eV) was evaluated using the sum of the optical band gap (E_g) and the HOMO level. The deeper HOMO level of **BEDCE** compared to Spiro-OMeTAD (-5.22 eV) can be expected to promote hole-injection from perovskite crystals. The hole mobilities of pristine **BEDCE** and Spiro-OMeTAD films were assessed by the space-charge limited current method (SCLC) on hole-only devices of structure indium tin oxide (ITO)/poly(3,4-ethylenedioxythiophene): polystyrene sulfonate (PEDOT:PSS)/**BEDCE**/MnO₃/Au (Fig. 1d). Spiro-OMeTAD was chemically doped in the same way as in PSCs (See Method). As shown in Table 1, **BEDCE** presents a higher mobility than that of Spiro-OMeTAD namely 4.35×10^{-4} vs $2.99 \times 10^{-4} \text{ cm}^2 \text{ V}^{-1} \text{ s}^{-1}$, respectively, indicating the excellent hole transporting capability.

Table 1 UV-Vis absorption, cyclic voltammetric data, energy levels and hole mobility of **BEDCE**. ^a in CHCl_3 , ^b film, ^c in 0.10 M $\text{Bu}_4\text{NPF}_6/\text{DCM}$, scan rate 50 mV s^{-1} , reference SCE.

Compd.	BEDCE
$\lambda_{\text{max}}^{\text{a}}$ (nm)	284, 338, 446
ϵ ($\text{M}^{-1} \text{cm}^{-1}$)	90000, 63000, 18000
$\lambda_{\text{max}}^{\text{b}}$ (nm)	288, 340, 448
$E_{\text{pa}1}, E_{\text{pa}2}^{\text{c}}$ (V)	0.75, 0.93
HOMO (eV)	-5.28
LUMO (eV)	-2.91
μ_{h} ($\text{cm}^2 \text{ V}^{-1} \text{ s}^{-1}$)	4.35×10^{-4}

In addition, it is also recognized that a uniform and smooth morphology is highly favored for improving the performance of PSCs.^{45,46} In particular, the grain boundaries of $\text{CH}_3\text{NH}_3\text{PbI}_3$ layer and pinholes in the Spiro-OMeTAD layer caused by the crystallization process, should be inhibited or otherwise passivated by an interfacial layer^{47–50}. The role of **BEDCE** layer in improving the microstructural quality can be seen clearly in Fig. 2, showing the scanning electron microscopy (SEM) images surface morphology of pure perovskite film, perovskite/Spiro-OMeTAD film, perovskite/**BEDCE** film, and perovskite/**BEDCE**/Spiro-OMeTAD film. The boundaries of $\text{CH}_3\text{NH}_3\text{PbI}_3$ crystals are obvious shown in Fig. 2a. The deposition of Spiro-OMeTAD on perovskite crystals leads to a smoother morphology, but the surface exhibits pinholes attributed to the strong tendency of Spiro-OMeTAD to crystallize (Fig. 2b). In contrast, when deposited on $\text{CH}_3\text{NH}_3\text{PbI}_3$ crystals, **BEDCE** forms a continuous smooth surface (Fig. 2c). Finally, as shown in Fig. 2d, the deposition of Spiro-OMeTAD on a thin **BEDCE** film leads to an improved homogeneity and compactness of the surface morphology, and free of any pinhole.

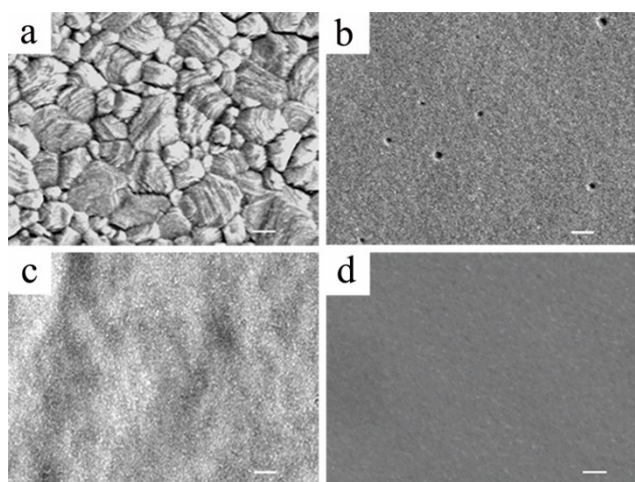
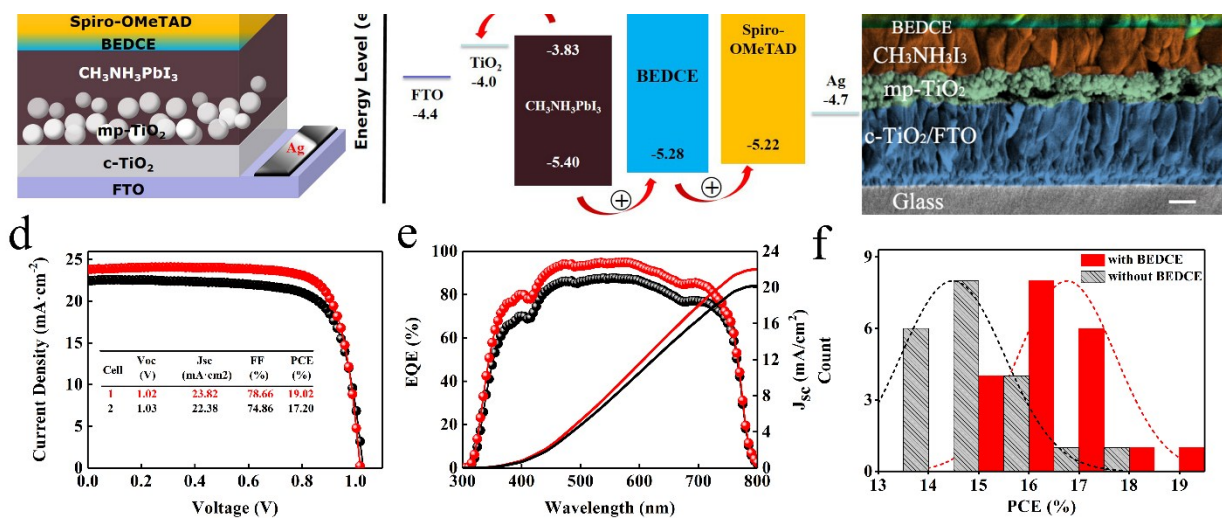


Fig. 2 Morphology characterizations. Top-view SEM images of a) pure perovskite film. b) Spiro-OMeTAD on perovskite. c) BEDCE on perovskite. d) perovskite/BEDCE/Spiro-OMeTAD. Scale bar: 200 nm.

The remarkably improved morphology is most likely associated with the fact that the elastomeric appearance of **BEDCE** allows a soft contact with Spiro-OMeTAD. Furthermore, the interface between the **BEDCE** and Spiro-OMeTAD layers also allows an opportunity for formation of an interfacial phase during the subsequent device fabrication. These two factors together limit effectively the fast crystallization process of the above Spiro-OMeTAD, yielding smoother and denser layer morphology. The underlying mechanism can be explained by looking into the water contact angle of Spiro-OMeTAD layer and **BEDCE** layer respectively deposited on perovskite layer, as shown in Fig. S8 in the Supporting Information. The contact angles, namely 85.4° vs 83.5° for the **BEDCE** and Spiro-OMeTAD layers deposited on top of the perovskite layers, respectively, indicate that **BEDCE** is a little less hydrophilic than Spiro-OMeTAD. As shown in previous work on materials based on triaryl amines, the long oligo-oxyethylene side chain substitution induced amphiphilic property of the resulting materials⁵¹. This unexpected result suggests that the hydrophilic oligo-oxyethylene chains are pointing downwards to the perovskite and forming a tight contact between **BEDCE** and perovskite layers, promoting the charge separation and transportation process in the perovskite layer and thus the whole structure.

BEDCE as interfacial layer in PSCs

Fig. 3 Illustrations and photovoltaic properties of PSCs. a) Schematic architecture of PSCs. b) Corresponding energy level diagrams of the materials used in the devices. c) SEM cross-sectional image of cell 1. *J* vs *V* characteristics d) and *EQE* spectra e) for best perovskite solar cells without **BEDCE** (Cell 2) and with a 10 nm as interfacial layer of **BEDCE** (Cell 1). f) Distribution histograms of PCEs for all of the cells with and without **BEDCE** layer.



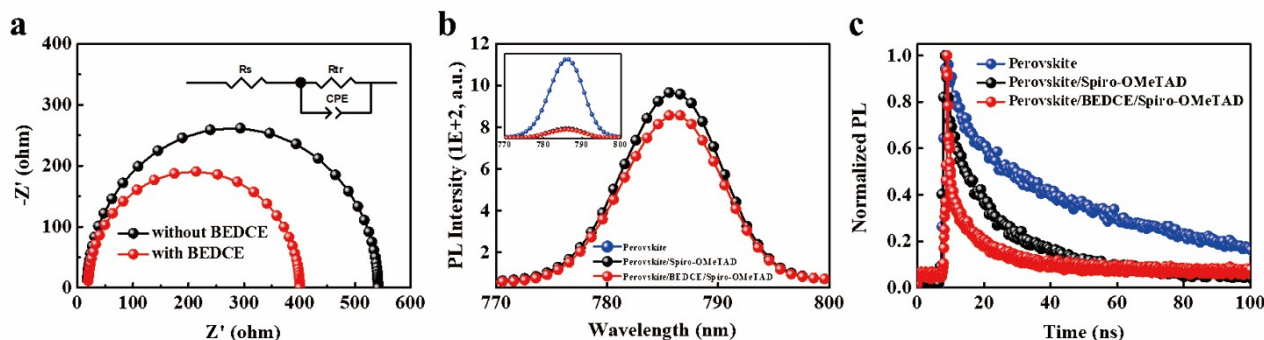


Fig. 4 Interfacial charge transporting properties characterization. a) Nyquist plots of cells 1 (red line) and 2 (black line), measured under dark ambient conditions at 200 mV applied bias. The inset shows the equivalent circuit. PL spectra b) and TRPL decay curves c) for films of perovskite, perovskite/Spiro-OMeTAD and perovskite/BEDCE/Spiro-OMeTAD on glass. Inset in b is the whole PL spectra.

Fig. 3d shows the current density-voltage (J - V) characteristics of the best cells with or without **BEDCE** under AM 1.5 simulated solar illumination with an incident power light of 100 mW cm^{-2} . The detailed photovoltaic parameters exhibiting the typical Gaussian distribution, are summarized in Fig. 3f and Fig. S10 (shown in Supporting Information). The reference cell 2 gives a best PCE of 17.20% with an open-circuit voltage (V_{OC}) of 1.03 V, a short-circuit current density (J_{SC}) of 22.38 mA cm^{-2} and a FF of 74.86%. The insertion of a thin layer of **BEDCE** between perovskite crystals and Spiro-OMeTAD leads to significant improvement in photovoltaic characteristics with a V_{OC} of 1.02 V, a J_{SC} of 23.83 mA cm^{-2} , and a FF of 78.66%, leading to a PCE of 19.02%. As expected, the smooth and pinhole-free morphology led by the insertion of **BEDCE** (Fig. 2d) gives a higher FF .

As shown in Fig. 3e, both devices present external quantum efficiencies (EQE) higher than 80% in the 450 - 650 nm spectral range. The insertion of the **BEDCE** layer leads to an improved response over the entire spectrum. Integration of these EQE spectra gives a J_{SC} increasing from 20.16 mA cm^{-2} for the cell devoid of **BEDCE** to 21.99 mA cm^{-2} upon insertion of the **BEDCE** layer. These values are in good agreement with the results obtained under white light illumination. The results of electrochemical impedance spectrometry (EIS) (Fig. 4a) show that the introduction of a 10 nm layer of **BEDCE** in the device induces a net decrease of the transfer resistance (R_{tr}) which is the characteristic arc obtained in the high frequency ($10^4 - 10^6$ Hz), illustrating the lower electron-hole recombination rate at perovskite/**BEDCE**/Spiro-OMeTAD interfaces. This result, consistent with surface morphologies (Fig. 2), could explain the observed increase of FF .

The effect of the interfacial hole-transporting layers on the photoluminescence of $\text{CH}_3\text{NH}_3\text{PbI}_3$ has been investigated by steady-state photoluminescence emission spectroscopy (PL) and time-resolved photoluminescence (TRPL) on the films of perovskite, perovskite/Spiro-OMeTAD and perovskite/**BEDCE**/Spiro-OMeTAD films on glass. Excitation wavelengths of 520 and 472 nm were used for PL and TRPL, respectively. As shown in Fig. 4b, the strong emission peak of

$\text{CH}_3\text{NH}_3\text{PbI}_3$ at 770 - 800 nm is quenched to a large extent by the deposition of Spiro-OMeTAD. The insertion of the **BEDCE** interfacial layer produces a further quenching of photoluminescence, demonstrating that the photo-generated holes are efficiently extracted by the composite **BEDCE**/Spiro-OMeTAD hole-transporting layer and contributing to the higher J_{SC} and FF . This conclusion is further confirmed by TRPL measurements (Fig. 4c). The TRPL signal exhibits a bi-exponential decay with a shorter-lived lifetime τ_1 of 9.18 ns and a longer-lived lifetime τ_2 of 73.64 ns for pristine perovskite film. These values are reduced to 4.24 ns and 21.59 ns after deposition of Spiro-OMeTAD and further reduced to 1.09 ns and 12.60 ns after insertion of a **BEDCE** layer between Spiro-OMeTAD and the perovskite film. This result is in accordance with the PL results and suggestion of a faster charge-transfer after insertion a layer of **BEDCE**.

The stability tests of PSCs with or without **BEDCE** were conducted with the humidity around 35% (Fig. S11, Supporting Information). In two weeks, no obvious degradation was observed. In addition, taking the blocking property of **BEDCE** from ion diffusion of the Spiro-OMeTAD layer into account, the even longer stability could be obtained.

BEDCE as An Emitter in Solution-Processed OLEDs

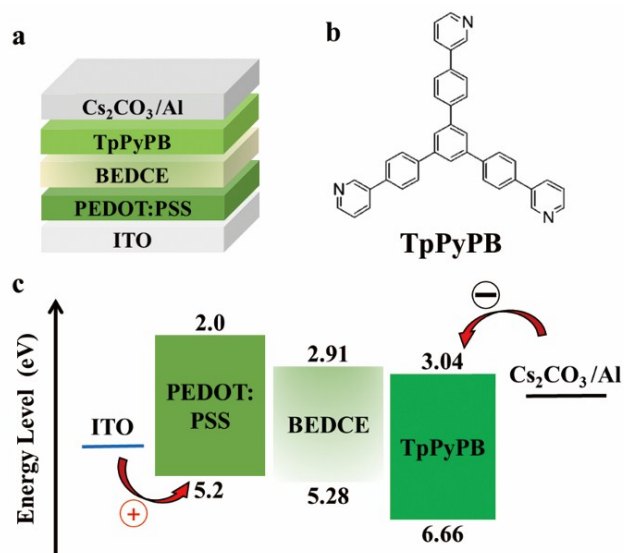


Fig. 5 Illustration of BEDCE based OLED. a) Architecture of the OLED. b) Molecular structures of ETL. c) Energy levels of OLED components.

In order to evaluate the potential of **BEDCE** as an emitter in solution-processed non-doped OLEDs, an OLED of structure ITO/PEDOT: PSS (40 nm)/**BEDCE**/TpPyPB (50 nm)/Cs₂CO₃ (1 nm)/Al (100 nm) was fabricated (Fig. 5a), where ITO was the anode, PEDOT: PSS was the hole injection/transport layer, **BEDCE** was the greenish-yellow emitter, Cs₂CO₃ was the electron injection layer, and Al was the cathode. After a careful selection of electron transporting layer (ETL), 1,3,5-tri(*p*-pyrid-3-yl-phenyl)benzene (TpPyPB) was used (Fig. 5b)⁵², owing to i) its ultrahigh electron mobility of $7.9 \times 10^{-3} \text{ cm}^2 \cdot \text{V}^{-1} \cdot \text{s}^{-1}$, which can efficiently transport electrons; ii) deep HOMO of -6.66 eV , which can effectively prevent the holes leakage. The HOMO and LUMO energy levels of these materials are shown in Fig. 5c. The high hole-mobility and small HOMO barrier with PEDOT: PSS (0.08 eV)⁵³ of **BEDCE** allow holes to effectively reach the emitting layer⁵⁴. Moreover, the elastomeric appearance and the amphiphilic property of **BEDCE** make it easy to form a better interfacial contact with the beneath PEDOT: PSS and the above TpPyPB, favoring the charge injection into the emitting layer.

As shown in Fig. 6a, the maximum current efficiency (CE) and EQE of 4.56 cd A^{-1} and 1.34 % are obtained, respectively. A maximum power efficiency (PE) of 2.05 lm W^{-1} is measured (Fig. S12, Supporting Information) with a maximum luminance 10320 cd m^{-2} (Fig. 6b). The electroluminescence (EL) spectrum of **BEDCE** is shown in Fig. 6c and the Commission International de l'Éclairage (CIE) coordinates of (0.36, 0.59) is displayed in Fig. 6d. Since this CIE coordinate is far away from that of National Television System Committee (NTSC) for green color (0.21, 0.71), it can be attributed to greenish-yellow emission according to previous reports^{43,55-58}. These results show that an efficient and bright solution-processed greenish-yellow OLED has been fabricated. To the best of our knowledge, this is the first OLED based on elastomeric ICZ materials. Furthermore, the efficiency and luminance are among the highest reported so far

for solution-processed non-doped greenish-yellow fluorescent OLEDs. By further enhancing molecular engineering and device engineering (e.g., optimizing the charge balance via the selection of ETL with higher LUMO to reduce the electron transport barrier, improving the hole transport into the active layer by using more suitable hole injection layer), much higher efficiency can be expected. These facts suggest that further molecular engineering could lead to interesting new emitting materials derived from this ICZ basic structure.

Conclusions

In summary, an efficient and multi-functional ICZ-based compound has been successfully synthesized in good yield by a three-step method. The grafting of four polyether side chains

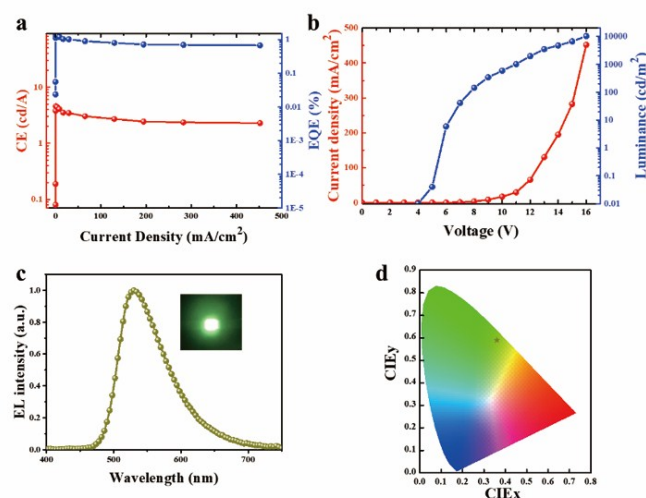


Fig. 6 Characterization of the OLED. a) CE and EQE. b) Current density and luminance. c) EL spectrum at 1000 cd m^{-2} (Inset: photograph of device at 1000 cd m^{-2}). d) CIE coordinates.

on the molecule confers an amphiphilic and elastomeric properties to the resulting **BEDCE** material. The insertion of a thin interfacial layer of **BEDCE** between perovskite and the classical Spiro-OMeTAD hole-transporting material ensures the full coverage of perovskite crystals and the filling of crystal boundaries resulting in the elimination of pinholes in the fast crystallized Spiro-OMeTAD, with an increase of FF from 74.86 % to 78.66 % and of PCE 17.20 % to 19.02 %. Besides, based on its high Φ_{PL} **BEDCE** has been used as emitting material in solution-processed non-doped greenish-yellow OLEDs with efficiency and luminance (4.56 cd A^{-1} and 10320 cd m^{-2}) among the highest reported so far for this kind of device. These results demonstrate that **BEDCE** and related compounds can represent efficient multi-functional materials with a large potential for light-electricity interconversion devices.¹⁻³

Methods

Materials and characterization

Chemical reagents were purchased and used as received without further purification. Tetrahydrofuran (THF) was distilled in presence of sodium and benzophenone under protection of dry nitrogen prior to use. NMR spectra were recorded on Bruker Avance or a Varian as 400 MHz spectrometer (^1H , 400 MHz and ^{13}C 100 MHz) using CDCl_3 or DMSO- d_6 as solvent and tetramethylsilane (TMS) as an internal standard. UV-Vis spectra were recorded with a PerkinElmer LAMBDA 950 UV/Vis/NIR Spectrophotometer. Photoluminescence (PL) spectra were measured with a HITACHI F-4600 spectrofluorometer. DSC experiments were recorded on a METTLER TOLEDO instrument with scanning rate of 10 K/min.

Mobility Measurements

The devices were fabricated according to literature procedures. The detailed device fabrication follows: ITO-coated glass as substrates was patterned. The substrates were carefully washed in ultrasonic baths of detergents, deionized water, acetone, isopropanol, and plasma. A PEDOT: PSS layer was deposited onto the substrates by spin-coating at a speed of 4000 rpm for 1 min; then the substrates were sintered at 120 °C for 30 min in air. The undoped HTMs (15 mg mL^{-1}) were dissolved in anhydrous dichloromethane. The HTM solution was spun-cast on the above substrates at a speed of 2000 rpm. Dektak 6M profilometer was used to measure the thicknesses of the films. Finally, molybdenum oxide (15nm) and gold (60 nm) were thermally evaporated under high vacuum on the HTM layer. J–V characteristics of the devices have been measured with a Keithley 2400 Source-Measure unit, interfaced with a computer. Device characterization was carried out in air.

Solar Cells Fabrication

Devices were prepared on transparent FTO (Pilkington, TEC-8, 8 $\Omega\text{-sq}^{-1}$) coated glass substrates which were ultrasonically cleaned with detergent, deionized water, acetone and isopropanol for 15 min, sequentially, followed by plasma cleaning for 10 min prior to use. A compact titanium dioxide (TiO_2) layer was spun-cast from a solution of 0.15 M titanium diisopropoxide di(acetylacetonate) (SigmaAldrich, 75 wt % in isopropanol) in 1-butanol (Sigma-Aldrich, 99.8 %) at 2000 rpm for 30 s on the pre-cleaned FTO, followed by drying at 125 °C for 10 min. After cooling down, mesoporous TiO_2 layer was deposited by spin-coating the TiO_2 paste (Dyesol 18NR-T) diluted in anhydrous ethanol (1:7 w/w) at 5000 rpm for 30 s, followed by drying at 125 °C for 10 min. The layers were annealed at 500°C for 30 min in muffle furnace. Once cooled and it was plasma treated for 10 min prior to use. The $\text{CH}_3\text{NH}_3\text{PbI}_3$ precursor solution was prepared in a glovebox by 1.25 M PbI_2 and 1.26 M MAI in the mixed solution of N,N-dimethylformamide (DMF, 99.8 %, anhydrous, Sigma-Aldrich) and dimethylsulfoxide (DMSO, 99.8 %, anhydrous, Sigma-Aldrich) (7:3 v/v). The spin-coating procedure was performed by 500 rpm for 3 s followed with 5000 rpm for 30 s. At 20 s before the last spin-casting step, 420 μL of chlorobenzene was pipetted

onto the rotating substrate, followed by annealing at 100°C for 10 min on the hotplate. 20 μL of BEDCE solution of 10 mg in 1 mL chlorobenzene was spin-cast on the top of perovskite at 500 rpm for 3 s followed with 3000 rpm for 30 s. Subsequently, 20 μL of spiro-OMeTAD solution (72 mg in 1 mL chlorobenzene, Toronto Research Chemicals), 29 μL of 4-tert-butyl pyridine (Sigma-Aldrich, 96 %) and 17.5 μL of lithiumbis(trifluoromethanesulfonyl)imide (Li-TFSI) solution (520 mg Li-TFSI in 1 mL acetonitrile (Sigma-Aldrich, 99.8 %) were mixed together and was spin-cast at 2000 rpm for 30 s. Devices were finalized by thermal evaporation of 100 nm thick Ag layer at a constant evaporation rate of $1 \text{ \AA}\cdot\text{s}^{-1}$. The active area of all devices was 0.07 cm^2 defined by a metal mask.

Characterizations of Solar Cells

The current-voltage (J-V) curves of the devices were measured by Keithley 2400 in a glovebox under AM1.5G illuminations (1000 W m^{-2}) from a solar simulator (Newport, 91160), which was calibrated using a standard silicon solar cell device by the NREL. The external quantum efficiency (EQE) curves were measured using a standard EQE system (Newport 66902). Electrochemical impedance spectroscopy (EIS) measurements were carried out in the dark by CHI6601 Electrochemical Workstation that bias voltage 200 mV with a 5 mV voltage perturbation was applied for the measurements over a frequency range of 10^{-1} – 10^6 Hz (from the highest to the lowest). Scanning electron microscope (SEM) images were obtained by FE-SEM (ZEISSUltra55). Steady-state photoluminescence (PL) spectra (HORIBA fluorolog-3) were measured under an excitation wavelength of 520 nm. Time-resolved photoluminescence (TRPL) measurements were performed on FLS980 at room temperature with excitation wavelength 472 nm. The contact angle measurements were obtained by OCA 15 Procontact-angle system (Dataphysics, Germany) using a 2 μL droplets at room temperature.

OLEDs Fabrication

AI4083 PEDOT: PSS solutions (filtered through a 0.45 μm filter) were spin-cast onto the ITO-coated glass substrates at 4000 rpm for 60 s and baked at 150 °C for 30 min. BEDCE was deposited by spin-casting at 2000 rpm for 30 s. Afterward, the samples were transferred into a vacuum thermal evaporation chamber to deposit other organic materials and cathode. Without breaking the vacuum, the electron transporting layer, Cs_2CO_3 and Al layers were thermally deposited at a base pressure of 2.0×10^{-4} Pa. The thicknesses of layers were controlled by the quartz crystal oscillators. After preparation all devices were immediately encapsulated under a nitrogen atmosphere using epoxy glue and glass slides. The emission area of all devices is $1 \times 1 \text{ mm}^2$ as defined by the overlapping area of the anode and cathode. The CIE coordinates and EL spectra were recorded via a PR705 Spectra Scan spectrometer using a computer-controlled source meter, the current density-voltage-luminance properties were measured simultaneously.

Conflicts of interest

There are no conflicts to declare.

Acknowledgements

We thank the financial support from National Key R&D Program of China (No. 2016YFA0201002), Guangdong Provincial Foundation (2016KQNCX035), NSFC grant (No. 51803064, 51571094, 51431006, 51561135014, U1501244), Program for Chang Jiang Scholars and Innovative Research Teams in Universities (No. IRT_17R40) and Guangdong Innovative Research Team Program (No. 2013C102). We also thank the support from the Guangdong Provincial Engineering Technology Research Center for Transparent Conductive Materials, National Center for International Research on Green Optoelectronics (IrGO), MOE International Laboratory for Optical Information Technologies and the 111 Project, and University Foundation (16KJ06). This work was in part, financially supported by the project SMOSCs (37_220).

Supplemental information

Supplemental information includes 8 figures, synthetic details and NMR spectra and can be found with this article online.

Author contributions

R. M. and X. W. contributed equally. Y. J. and J. W. G conceived and co-directed the project. Y. J. and R. M. designed and synthesized the materials. X. W. fabricated and optimized the PSCs device. B. L. fabricated and optimized the OLEDs devices. Y. M. and X. H. contributed to the materials characterization. Y. J., J. G., B. L., J. R., K. K. contributed to the writing. J.-M. L. and G. Z. participated in the results discussion. All authors commented on the final paper.

Corresponding Author

*E-mail for Y. J.: yuejiang@m.scnu.edu.cn

*E-mail for B. L.: bqliu@ntu.edu.sg

*E-mail for J. R.: jeanroncali@gmail.com

*E-mail for J. G.: gaojw@m.scnu.edu.cn

References

- R. H. Friend, Gymer, R. W., Holmes, A. B., Burroughes, J. H., Marks, R. N., Taliani, C., Bradley, D. D. C., Santos, D. A. D., Brédas, J. L., Lögdlund, M., and Salaneck, W. R., *Nature* 1999, **397**, 121-128.
- A. L. Kanibolotsky, I. F. Perepichka and P. J. Skabara, *Chem. Soc. Rev.*, 2010, **39**, 2695-2728.
- J. Cao, Q. Liao, X. Du, J. Chen, Z. Xiao, Q. Zuo and L. Ding, *Energ. Environ. Sci.*, 2013, **6**, 3224.
- Y. Chen, Wan, X., and Long, G., *Accounts Chem. Res.*, 2013, **46**, 2645-2655.
- Y. Lin, Y. Li and X. Zhan, *Chem. Soc. Rev.*, 2012, **41**, 4245-4272.
- A. Mishra and P. Bauerle, *Angew. Chem. Int. Ed. Engl.*, 2012, **51**, 2020-2067.
- J. Roncali, P. Leriche and P. Blanchard, *Adv. Mater.*, 2014, **26**, 3821-3838.
- L. Duan, J. Qiao, Y. Sun and Y. Qiu, *Adv. Mater.*, 2011, **23**, 1137-1144.
- J. Guo, X.-L. Li, H. Nie, W. Luo, S. Gan, S. Hu, R. Hu, A. Qin, Z. Zhao, S.-J. Su and B. Z. Tang, *Adv. Funct. Mater.*, 2017, **27**, 1606458.
- M. Y. Wong and E. Zysman-Colman, *Adv. Mater.*, 2017, **29**, 1605444.
- S. Allard, M. Forster, B. Souharce, H. Thiem and U. Scherf, *Chem. Int. Ed. Engl.*, 2008, **47**, 4070-4098.
- Y. Gao, Y. Deng, H. Tian, J. Zhang, D. Yan, Y. Geng and F. Wang, *Adv. Mater.*, 2017, **29**.
- J. H. Park, H. S. Lee, S. Park, S.-W. Min, Y. Yi, C.-G. Cho, J. Han, T. W. Kim and S. Im, *Adv. Funct. Mater.*, 2014, **24**, 1109-1116.
- I. García-Benito, I. Zimmermann, J. Urieta-Mora, J. Aragó, J. Calbo, J. Perles, A. Serrano, A. Molina-Ontoria, E. Ortí, N. Martín and M. K. Nazeeruddin, *Adv. Funct. Mater.*, 2018, **28**, 1801734.
- P.-L. T. Boudreault, Wakim, S., Blouin, N., Simard, M., Tessier, C., Tao, Y., and Leclerc, M., *J. Am. Chem. Soc.*, 2007, **129**, 9125-9136.
- I. Petrikyte, I. Zimmermann, K. Rakstys, M. Daskeviciene, T. Malinauskas, V. Jankauskas, V. Getautis and M. K. Nazeeruddin, *Nanoscale*, 2016, **8**, 8530-8535.
- D. Zhang, X. Song, M. Cai, H. Kaji and L. Duan, *Adv. Mater.*, 2018, **30**, 1705406.
- C.-C. Lai, M.-J. Huang, H.-H. Chou, C.-Y. Liao, P. Rajamalli and C.-H. Cheng, *Adv. Funct. Mater.*, 2015, **25**, 5548-5556.
- P. B. W. Yang W S, Jung E H, *Science*, 2017, **356**, 1376-1379.
- http://www.nrel.gov/ncpv/images/efficiency_chart.jpg.
- O. Ostroverkhova, *Chem. Rev.*, 2016, **116**, 13279-13412.
- C. H. Teh, R. Daik, E. L. Lim, C. C. Yap, M. A. Ibrahim, N. A. Ludin, K. Sopian and M. A. Mat Teridi, *J. Mater. Chem. A*, 2016, **4**, 15788-15822.
- Z. Hawash, L. K. Ono, S. R. Raga, M. V. Lee and Y. Qi, *Chem. Mater.*, 2015, **27**, 562-569.
- M. Salado, J. Idigoras, L. Calio, S. Kazim, M. K. Nazeeruddin, J. A. Anta and S. Ahmad, *ACS Appl. Mater. Interfaces*, 2016, **8**, 34414-34421.
- T. P. I. Saragi, Spehr, T., Siebert, A., Fuhrmann-Lieker, T., and Salbeck, J., *Chem. Rev.*, 2007, **170**, 1011-1065.
- J. Liu, Y. Wu, C. Qin, X. Yang, T. Yasuda, A. Islam, K. Zhang, W. Peng, W. Chen and L. Han, *Energ. Environ. Sci.*, 2014, **7**, 2963-2967.
- M. L. Petrus, T. Bein, T. J. Dingemans and P. Docampo, *J. Mater. Chem. A*, 2015, **3**, 12159-12162.
- P. Qin, H. Kast, M. K. Nazeeruddin, S. M. Zakeeruddin, A. Mishra, P. Bauerle and M. Grätzel, *Energ. Environ. Sci.*, 2014, **7**, 2981-2985.
- B. Xu, Bi, D., Hua, Y., Liu, P., Cheng, M., Grätzel, M., Kloo, L., Hagfeldt, A., and Sun, L., *Energ. Environ. Sci.*, 2016, **9**, 873-877.
- L. Calió, Kazim, S., Grätzel, M., and Ahmad, S., *Angew. Chem. Int. Edit.*, 2016, **55**, 14522-14545.
- Y. Song, Lv, S., Liu, X., Li, X., Wang, S., Wei, H., Li, D., Xiao, Y., and Meng, Q., *Chem. Commun.*, 2014, **50**, 15239-15242.
- X. Yin, L. Guan, J. Yu, D. Zhao, C. Wang, N. Shrestha, Y. Han, Q. An, J. Zhou, B. Zhou, Y. Yu, C. R. Grice, R. A. Awni, F. Zhang, J. Wang, R. J. Ellingson, Y. Yan and W. Tang, *Nano Energy*, 2017, **40**, 163-169.
- H. Shi, J. Yuan, X. Wu, X. Dong, L. Fang, Y. Miao, H. Wang and F. Cheng, *New J. Chem.*, 2014, **38**, 2368.

- 34 C. Yin, J. Lu, Y. Xu, Y. Yun, K. Wang, J. Li, L. Jiang, J. Sun, A. D. Scully, F. Huang, J. Zhong, J. Wang, Y.-B. Cheng, T. Qin and W. Huang, *Adv. Energ. Mater.*, 2018, **8**, 1800538.
- 35 C. Lu, I. T. Choi, J. Kim and H. K. Kim, *J. Mater. Chem. A*, 2017, **5**, 20263-20276.
- 36 C. Liu, Z. Huang, X. Hu, X. Meng, L. Huang, J. Xiong, L. Tan and Y. Chen, *ACS Appl. Mater. Interfaces*, 2018, **10**, 1909-1916.
- 37 A. Fakharuddin, L. Schmidt-Mende, G. Garcia-Belmonte, R. Jose and I. Mora-Sero, *Adv. Energ. Mater.*, 2017, **7**, 1700623.
- 38 F. Wang, A. Shimazaki, F. Yang, K. Kanahashi, K. Matsuki, Y. Miyauchi, T. Takenobu, A. Wakamiya, Y. Murata and K. Matsuda, *J. Phys. Chem. C*, 2017, **121**, 1562-1568.
- 39 P.-Y. Su, Huang, L.-B., Liu, J.-M., Chen, Y.-F., Xiao, L.-M., Kuang, D.-B., Mayor, M., and Su, C.-Y., *J. Mater. Chem. A*, 2017, **5**, 1913-1918.
- 40 D. Song, Wei, D., Cui, P., Li, M., Duan, Z., Wang, T., Ji, J., Li, Y., Mbengue, J. M., Li, Y., He, Y., Trevor, M., and Park, N.-G., *J. Mater. Chem. A*, 2016, **4**, 6091-6097.
- 41 X. L. Li, G. Xie, M. Liu, D. Chen, X. Cai, J. Peng, Y. Cao and S. J. Su, *Adv. Mater.*, 2016, **28**, 4614-4619.
- 42 Y. Shirasaki, G. J. Supran, M. G. Bawendi and V. Bulović, *Nature Photonics*, 2013, **7**, 13-23.
- 43 H. Shi, J. Yuan, X. Dong and F. Cheng, *Spectrochimica acta. Part A, Molecular and biomolecular spectroscopy*, 2014, **133**, 501-508.
- 44 H. A. Gu R, Dehaen W, *J. Org. Chem.*, 2007, **72**, 7207-7213.
- 45 Z. Huang, X. Hu, C. Liu, L. Tan and Y. Chen, *Adv. Funct. Mater.*, 2017, **27**, 1703061.
- 46 Q. Fu, X. Tang, B. Huang, T. Hu, L. Tan, L. Chen and Y. Chen, *Adv. Sci.*, 2018, **5**, 1700387.
- 47 S. Kazim, Ramos, F. J., Gao, P., Nazeeruddin, M. K., Grätzel, M., and Ahmad, S., *Energ. Environ. Sci.*, 2015, **8**, 1816-1823.
- 48 J. Carrillo, A. Guerrero, S. Rahimnejad, O. Almora, I. Zarazua, E. Mas-Marza, J. Bisquert and G. Garcia-Belmonte, *Adv. Energ. Mater.*, 2016, **6**, 1502246.
- 49 Y. Li, Ji, L., Liu, R., Zhang, C., Mak, C. H., Zou, X., Shen, H.-H., Leu, S.-Y., and Hsu, H.-Y., *J. Mater. Chem. A*, 2018, **6**, 2842-12875.
- 50 C. Steck, M. Franckevičius, S. M. Zakeeruddin, A. Mishra, P. Bäuerle and M. Grätzel, *J. Mater. Chem. A*, 2015, **3**, 17738-17746.
- 51 Y. Jiang, D. Gindre, M. Allain, P. Liu, C. Cabanetos and J. Roncali, *Adv. Mater.*, 2015, **27**, 4285-4289.
- 52 S.-J. Su, T. Chiba, T. Takeda and J. Kido, *Adv. Mater.*, 2008, **20**, 2125-2130.
- 53 M. D. Irwin, D. B. Buchholz, A. W. Hains, R. P. H. Chang and T. J. Marks, *Proceedings of the National Academy of Sciences*, 2008, **105**, 2783-2787.
- 54 B. Liu, H. Tao, L. Wang, D. Gao, W. Liu, J. Zou, M. Xu, H. Ning, J. Peng and Y. Cao, *Nano Energy*, 2016, **26**, 26-36.
- 55 J.-H. Jou, Lin, Y.-X., Peng, S.-H., Li, C.-J., Yang, Y.-M., Chin, C.-L., Shyue, J.-J., Sun, S.-S., Lee, M., Chen, C.-T., Liu, M.-C., Chen, C.-C., Chen, G.-Y., Wu, J.-H., Li, C.-H., Sung, C.-F., Lee, M.-J., and Hu, J.-P., *Adv. Funct. Mater.*, 2014, **24**, 555-562.
- 56 S. Krotkus, D. Kasemann, S. Lenk, K. Leo and S. Reineke, *Light Sci. Appl.*, 2016, **5**, e16121.
- 57 E. Mondal, W.-Y. Hung, H.-C. Dai and K.-T. Wong, *Adv. Funct. Mater.*, 2013, **23**, 3096-3105.
- 58 P. Tao, W.-L. Li, J. Zhang, S. Guo, Q. Zhao, H. Wang, B. Wei, S.-J. Liu, X.-H. Zhou, Q. Yu, B.-S. Xu and W. Huang, *Adv. Funct. Mater.*, 2016, **26**, 881-894.